# Design of High-Performance Lead-Free Quaternary Antiperovskites for Photovoltaics via Ion Type Inversion and Anion Ordering

Dan Han[1*], Chunbao Feng[2], Mao-Hua Du[3], Tao Zhang[4], Shizhe Wang[1], Gang Tang[5*], Thomas Bein[1], Hubert Ebert[1]

[1]Department of Chemistry, University of Munich, Munich, D-81377, Germany

[2]School of Science, Chongqing University of Posts and Telecommunications, Chongqing 400065, China

[3]Materials Science & Technology Division, Oak Ridge, TN, 37831, USA

[4]Key Laboratory of Polar Materials and Devices (MOE), East China Normal University, Shanghai 200241, China

[5]Theoretical Materials Physics, Q-MAT, CESAM, University of Liège, B-4000 Liège, Belgium

Keywords: quaternary antiperovskite, photovoltaic absorber, optoelectronic properties, three-dimensional electronic transport, first-principles calculations

ABSTRACT: The emergence of halide double perovskites significantly increases the compositional space for lead-free and air-stable photovoltaic absorbers compared to halide perovskites. Nevertheless, most halide double perovskites exhibit oversized band gaps (> 1.9 eV) or dipole-forbidden optical transition, which are unfavorable for efficient single-junction solar cell applications. The current device performance of halide double perovskite is still inferior to that of lead-based halide perovskites, such as $CH_3NH_3PbI_3$ ($MAPbI_3$). Here, by ion-type inversion and anion ordering on perovskite lattice sites, two new classes of pnictogen-based quaternary antiperovskites with the formula of $X_6B_2AA'$ and $X_6BB'A_2$ are designed. Phase stability and tunable band gaps in these quaternary antiperovskites are demonstrated based on first-principles calculations. Further photovoltaic-functionality-directed screening of these materials leads to the discovery of 5 stable compounds ($Ca_6N_2AsSb$, $Ca_6N_2PSb$, $Sr_6N_2AsSb$, $Sr_6N_2PSb$, and $Ca_6NPSb_2$) with suitable direct band gaps, small carrier effective masses and low exciton binding energies, and dipole-allowed strong optical absorption, which are favorable properties for a photovoltaic absorber material. The calculated theoretical maximum solar cell efficiencies based on these five compounds are all larger than 29%, comparable to or even higher than that of the $MAPbI_3$ based solar cell. Our work reveals the huge potential of quaternary antiperovskites in the optoelectronic field and provides a new strategy to design lead-free and air-stable perovskite-based photovoltaic absorber materials.

**TOC Graphic:**

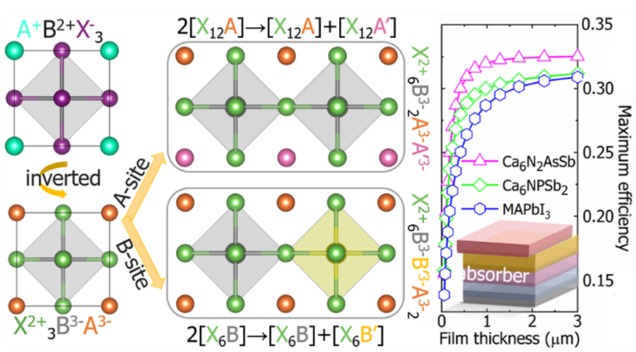

## 1. INTRODUCTION

Halide perovskites $ABX_3$ have attracted intense research interest due to their excellent optoelectronic properties.[1-3] Lead-based organic-inorganic hybrid halide perovskite solar cells have achieved a record power conversion efficiency (PCE) above 25% within only one decade, exhibiting a unprecedented rapid advancement of PCE.[4] Despite this exciting development, the toxicity of Pb and the poor intrinsic stability are the two main roadblocks for their further large-scale commercialization.[5-6] To solve the concern about toxic Pb, a straightforward method is to substitute Pb with other group-IVA metal elements Sn and Ge because they have the same valence electron configurations ($ns^2np^2$).[7-9] However, $Sn^{2+}$ and $Ge^{2+}$ are prone to oxidation, leading to rapid device degradation.[7, 10-11] Besides these group-IVA cations, other divalent cations without lone-pair s orbitals have been considered, but the resulting compounds display unfavorable properties for photovoltaic applications (such as oversized band gaps and poor carrier mobility).[12-13]

Recently, a promising strategy for eliminating Pb has been proposed, that is, transmuting two $Pb^{2+}$ ions into a monovalent ion $B^+$ and a trivalent ion $B'^{3+}$, forming a halide double perovskite $A_2BB'X_6$.[14-17] Halide double perovskites are a large family of compounds with broad structural and compositional flexibilities, which show better stability compared to lead-based organic-inorganic hybrid halide perovskites.[18-20] Hundreds of halide double perovskites have been screened via density functional theory in combination with high-throughput calculations,[16-17, 21-23] resulting in the discovery of several candidates as photovoltaic absorber materials, namely $Cs_2BB'X_6$ (B=In, Tl; B' =Sb, Bi; X=Cl, Br).[16, 23] However, these compounds suffer from several problems, including the oxidation of $In^+$ to $In^{3+}$,[24] and the high toxicity of Tl. Furthermore, to date, most of the synthesized lead-free halide double perovskites exhibit large indirect band gaps, or dipole-forbidden optical transitions between the valence and conduction band edges,[23, 25] which is undesirable for efficient applications in single-junction thin-film solar cells. Although methods such as alloying, doping and dimensionality reduction have been utilized for property tuning, favorable photovoltaic properties in halide double perovskites have not been obtained yet.[26-28] Currently, the highest PCE of a halide double perovskite ($Cs_2AgBiBr_6$) based solar cell is 3.11%,[29] which is still far below the PCE of the hybrid organic-inorganic lead halide perovskite solar cells (25.5%).[4]

Beyond the direct atomic substitution and cation transmutation, another interesting material design strategy based on the perovskite structure is forming electronically inverted antiperovskites compounds $X_3BA$.[30-36] They can be obtained by inverting the ion types on the respective lattice sites of cubic halide perovskites $ABX_3$, that is, two cationic species on the A- and B-sites become anionic ones, and one anionic species on the X-sites turn into cationic one. This strategy enables the exploration of a new compositional space. Compared to the intense research in halide perovskites and halide double perovskites, the studies on antiperovskite compounds for photovoltaic applications are still limited but have already shown promise. Gebhardt and coworkers predicted a series of organic-inorganic hybrid antiperovskites $(CH_3NH_3)_3BA$ (B and A sites are occupied by monovalent or divalent anions),[30-31] but the valence band (VB) and conduction band (CB) dispersions are small, suggesting inefficient carrier transport. On the other hand, all-inorganic antiperovskites $Ca_3NSb$, $Mg_3NSb$, $Mg_3(Ca/Sr)NP$ show suitable direct band gaps, dispersive VBs and CBs, and high optical absorption coefficients.[33-34, 37] The improved properties may be expected due to the enhanced covalency of pnictides.

Inspired by these works, starting from cubic halide perovskites $ABX_3$, we employed the strategies of ion-type inversion and anion ordering to design two new classes of quaternary antiperovskites with the formula of $X_6B_2AA'$ and $X_6BB'A_2$, where the X are alkaline-earth metals (Mg, Ca, Sr and Ba) and anions are a combination of pnictogen elements. Based on first-principles calculations, we systematically investigated their crystallographic and phase stabilities, and electronic structure trends. Note that halide-based B-site-ordered double antiperovskites ($Li_6O^{2-}S^{2-}I_2$) have previously been studied as solid electrolytes in ion batteries.[38] However, pnictogen-based quaternary antiperovskites have not been explored but may have a great potential for optoelectronic applications due to the enhanced covalency in pnictides (compared to halides and chalcogenides). By screening 48 quaternary antiperovskites based on criteria targeting specific thermodynamic, structural, and photovoltaic properties, we identified 5 new stable compounds which are environmentally friendly and display superior photovoltaic properties comparable to lead-based halide perovskites. Our designed quaternary antiperovskites increase the compositional space for the exploration of potential new optoelectronic materials with perovskite structures.

## 2. EXPERIMENTAL METHOD

First-principles calculations were performed using the Vienna Ab initio Simulation Package (VASP).[39] The generalized gradient approximation (GGA) in the Perdew-Burke-Ernzerhof (PBE) form was used for the exchange-correlation functional.[40] The kinetic-energy cutoff was chosen as 520 eV. The convergence criteria for the energy and force were set to $10^{-5}$ eV and 0.02 eV/Å, respectively. For the Brillouin zone integration, the Monkhorst-Pack k-point mesh with a grid spacing of $\sim 2\pi\times 0.03$ Å$^{-1}$ was used. A high-density k-point mesh (less than $2\pi\times 0.01$ Å$^{-1}$) was utilized for the calculation of optical absorption spectra. Hybrid functional (HSE) with the 25% non-local Fock exchange was employed for the band structure calculations.[41] The SOC effect was included because it affects strongly the electronic structure of compounds containing a heavy p-electron element like Bi.[42-43] Post-processing of band structures was performed using VASPKIT.[44]

The phase stability of 48 pnictogen-based quaternary antiperovskites was evaluated by calculating energy above hull ($E_{hull}$), namely the decomposition energy. We combined our calculated first-principles results of the targeted quaternary compounds with the data of all competing elementary substances, binary and ternary phases in the Materials Project database[45] (a Materials Genome database) to accelerate the evaluation of the thermodynamic stability. The total energy of targeted antiperovskites was calculated by adopting the same parameters used for generating energies of competing phases in Materials Project. The dynamic stability of a compound was assessed by calculating the phonon spectrum based on the frozen phonon method.[46] The effective mass was obtained by using finite difference method as implemented in Effective Mass Calculator (EMC).[47] The Wannier-Mott exciton binding energy ($E_b$) was estimated by using a modified hydrogen-atom-like Bohr model.[48] The theoretical conversion efficiency of solar cells was calculated based on the method proposed by Yu, L. et al and a python code (SL3ME).[49-50] To mimic the maximal anion disorder, 80-atom supercells for antiperovskites $Ca_6N_2AsSb$ and $Ca_6NPSb_2$ were constructed based on a special quasi-random structure (SQS) method.[51]

## 3. RESULTS AND DISCUSSION

### 3.1. Design Strategy and Stability of $X_6B_2AA'$ and $X_6BB'A_2$

The crystal structure of an antiperovskite $X_3BA$, which has a cationic X-site and two anionic A- and B-sites, is shown in Figure 1. Previous investigations of all-inorganic antiperovskites $X_3NA$ ($X^{2+}$ = Mg, Ca, Sr; $A^{3-}$ = P, As, Sb, Bi) revealed their favorable optoelectronic properties for photovoltaic applications.[33-34, 52] $X_3BA$ can be further transformed to quaternary antiperovskites ($X_6B_2AA'$ or $X_6BB'A_2$) by introducing anion ordering, viz., splitting the anionic A- or B-site, respectively, as shown in Figure 1. In this work, we considered 48 pnictogen-based quaternary antiperovskites: $X_6B_2AA'$ (B = N and AA' = PAs, PSb, AsSb, PBi, AsBi, SbBi) and $X_6BB'A_2$ (BB' = NP, NAs, PAs, and A = Sb, Bi).

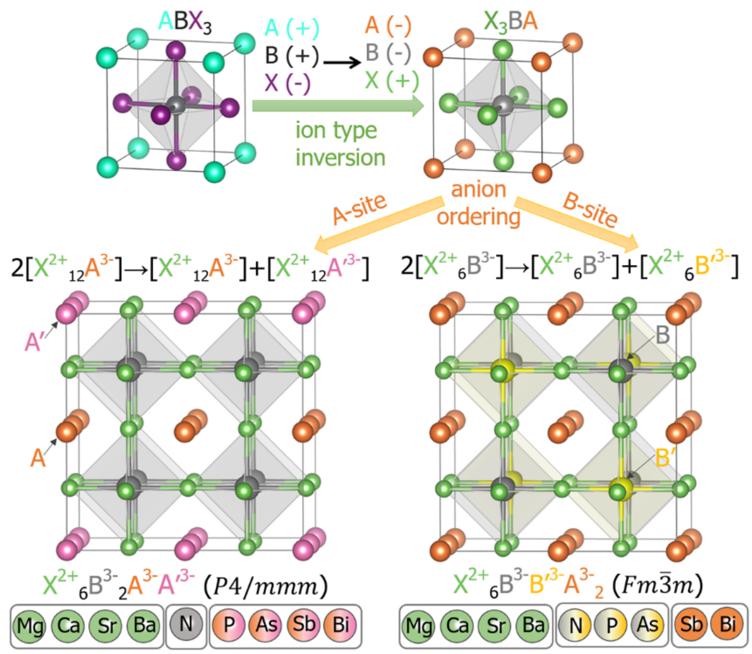


Figure 1. Schematic of quaternary antiperovskites ($X_6B_2AA'$ and $X_6BB'A_2$) derived from cubic halide perovskite and composition of $X_6B_2AA'$ and $X_6BB'A_2$ (X = Mg, Ca, Sr, Ba; for $X_6B_2AA'$, B = N, AA' = PAs, PSb, AsSb, PBi, AsBi, SbBi; for $X_6BB'A_2$, BB' = NP, NAs, PAs, and A = Sb, Bi).

We start by searching for the most energetically favored types of anionic orderings in $X_6B_2AA'$ and $X_6BB'A_2$. We construct a supercell by doubling the standard cubic distortion-free unit-cell of antiperovskite $X_3BA$, in which various arrangements of AA' and BB' anionic pairs are considered. There are 6 different configurations for both $X_6B_2AA'$ and $X_6BB'A_2$ (see configurations A, B, C, D, E, and F in Figure 2a). Figure 2a shows the calculated total energies of two A- ($Mg_6N_2SbBi$ and $Sr_6N_2AsBi$) and two B-site

($Mg_6NPSb_2$ and $Ca_6NAsBi_2$) ordered quaternary antiperovskites as typical examples. It can be seen that the most stable configuration of $X_6B_2AA'$ is the type A (*P*4*/mmm* phase), where the $[X^{2+}{}_{12}A^{3-}]$ and $[X^{2+}{}_{12}A'^{3-}]$ cuboctahedra alternate only along one crystallographic axis, forming the layered ordering. In contrast, for $X_6BB'A_2$, the configuration with the lowest energy is the type F ($Fm\overline{3}m$ phase), in which the $[X^{2+}{}_6B^{3-}]$ and $[X^{2+}{}_6B'^{3-}]$ octahedra alternate along three crystallographic axes, forming the rock-salt type ordering. The preferred configurations of A- and B-site-anion-ordering in quaternary antiperovskites are consistent with the cation ordering in conventional double perovskite oxides, where A-site cations favor the layered ordering while B-site cations prefer the rock-salt type ordering.[53] This is conceivable because an antiperovskite is merely electronically inverted from its perovskite counterpart. Additionally, some degrees of anion disorders especially on A/A' sites are possible owing to the slight energy difference between various configurations. The effect of anion disorder on the optoelectronic properties is discussed for the most promising compounds in Section 3.6. It should also be noted that the energy differences between different configurations of A-site-cation-ordered regular double pervoskites are small.[54]

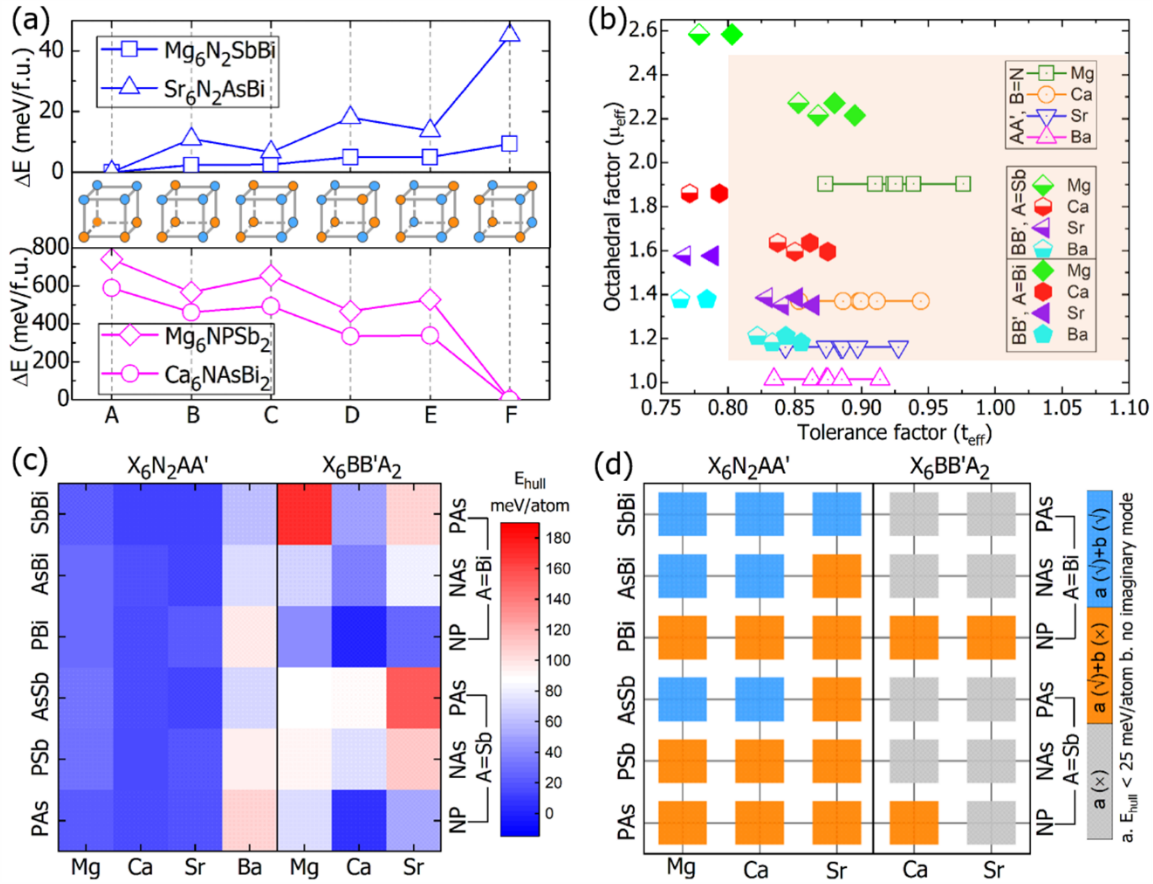

Figure 2. (a) Energies of $Mg_6N_2SbBi$, $Sr_6N_2AsBi$, $Mg_6NPSb_2$ and $Ca_6NAsBi_2$ in 6 configurations shown in the middle panel (light blue and orange balls represent [$X_{12}A$] and [$X_{12}A'$] cuboctahedra in $X_6B_2AA'$ or [$X_6B$] and [$X_6B'$] octahedra in $X_6BB'A_2$). The energy of the configuration with the lowest total energy is set to zero. (b) Distribution mapping of 48 quaternary antiperovskites with effective tolerance factor ($t_{eff}$) and octahedral factor ($\mu_{eff}$) as variables. (c) $E_{hull}$ of $X_6B_2AA'$ and $X_6BB'A_2$ compounds excluding $Ba_6BB'A_2$ of which large $E_{hull}$ are given in Table S1. These $E_{hull}$ are for compounds in tetragonal or cubic perovskite structures. (d) Mapping of dynamic stability of thermodynamically stable $X_6B_2AA'$ (space group (SG) *P*4/*mmm*) and $X_6BB'A_2$ (SG $Fm\bar{3}m$). A grey, orange, or blue square indicates that a compound is thermodynamically unstable ($E_{hull}$ > 25 meV), thermodynamically stable ($E_{hull}$ < 25 meV) but dynamically unstable (imaginary phonon modes), or stable both thermodynamically and dynamically ($E_{hull}$ < 25 meV and no imaginary phonon modes), respectively. Phonon spectra are shown in Figure S1 and S2.

To assess the crystallographic stability of $X_6B_2AA'$ and $X_6BB'A_2$, the empirical quantities based on the idealized solid-sphere model, i.e., the Goldschmidt tolerance (t) and octahedral factor (μ) are calculated. In light of the fact that there are few experimentally synthesized perovskite nitrides,[55] the (t, μ) range of halide and oxide perovskites was used as reference. On the other hand, it was suggested that tolerance factor region of stable cubic phase antiperovskite nitrides are wider than the antiperovskite oxides.[33] The statistical analysis of all the existing halide and oxide perovskites[56-57] suggests $0.81 < t < 1.11$ and $0.44 < \mu < 0.90$ for stable perovskites. One can define the effective tolerance factor ($t_{eff}$) and octahedral factor ($\mu_{eff}$) for quaternary antiperovskites $X_6B_2AA'$ and $X_6BB'A_2$ as follows,

$$t_{eff}\,(X_6B_2AA') = ((r_A + r_{A'})/2 + r_X)/\sqrt{2}(r_B + r_X) \;(1),$$

$$\mu_{eff}(X_6B_2AA') = r_B/r_X \;(2),$$

$$t_{eff}(X_6BB'A_2) = (r_A + r_X)/\sqrt{2}((r_B + r_{B'})/2 + r_X) \;(3),$$

$$\mu_{eff}(X_6BB'A_2) = (r_B + r_{B'})/2r_X \;(4),$$

where $r_X$, $r_A$, $r_{A'}$, $r_B$ in equation (1) and (2) are the ionic radii of $X^{2+}$, $A^{3-}$, $A'^{3-}$ and $B^{3-}$ ions in $X_6B_2AA'$, respectively. Similarly, $r_X$, $r_A$, $r_B$ and $r_{B'}$ in equation (3) and (4) are the ionic radii of $X^{2+}$, $A^{3-}$, $B^{3-}$ and $B'^{3-}$ ions in $X_6BB'A_2$, respectively. The ionic radii of $X^{2+}$ (Mg, Ca, Sr and Ba) are assigned using Shannon ionic radii and those of $N^{3-}$, $P^{3-}$, $As^{3-}$, $Sb^{3-}$, and $Bi^{3-}$ are from Ref.[33]. Since the ion type is inverted in antiperovskites, the range of μ becomes 1.11-2.27, while the range of t remains the same as that for perovskites. As shown in Figure 2b (a distribution mapping of quaternary antiperovskites with $t_{eff}$ and $\mu_{eff}$ as variables), we find that the majority of the compounds are within the empirically stable area of perovskites (the shaded area in Figure 2b) whilst 14 compounds including $Ba_6B_2AA'$ (AA' = PAs, PSb, AsSb, PBi, AsBi, SbBi) and $X_6PAsA_2$ (X = Mg, Ca, Sr, Ba; A = Sb, Bi) fall outside.

Beyond the crystallographic stability, we evaluated the thermodynamic stability of 48 pnictogen-based quaternary antiperovskites by calculating $E_{hull}$ of the targeted compound relative to all competing phases. For a given compound, a negative $E_{hull}$ indicates thermodynamic stability against decomposition. Among 48 pnictogen-based antiperovskites, only three compounds have negative $E_{hull}$, viz., $Ca_6N_2SbBi$ (−1 meV/atom), $Ca_6NPBi_2$ (−14 meV/atom) and $Ca_6NPSb_2$ (−8 meV/atom). Note that some metastable antiperovskites that are unstable at 0 K with small positive $E_{hull}$ have been synthesized experimentally at finite temperatures.[58-59] Accordingly, in this work, quaternary antiperovskites with $E_{hull}$ below 25 meV/atom (approximately $k_BT$ at room temperature) are labeled as thermodynamically stable considering the possibility of entropic stabilization. Following this criterion, as shown in Figure 2c and Table S1, for Mg-, Ca- and Sr-based quaternary antiperovskites, all of the A-site-ordered ones and three B-site-ordered ones ($Ca_6NPSb_2$, $Ca_6NPBi_2$ and $Sr_6NPBi_2$) are stable; however, none of the Ba-based quaternary antiperovskites are thermodynamically stable. Note that the 14 compounds without crystallographic stability as shown in Figure 2b have rather large $E_{hull}$, indicating their thermodynamical instability.

In addition to the thermodynamic stability, the dynamic stability of 21 thermodynamically stable compounds was assessed. Seven A-site-ordered quaternary antiperovskites in the $P4/mmm$ symmetry ($Mg_6N_2AsSb$, $Mg_6N_2AsBi$, $Mg_6N_2SbBi$, $Ca_6N_2AsSb$, $Ca_6N_2AsBi$, $Ca_6N_2SbBi$ and $Sr_6N_2SbBi$) show no imaginary modes as displayed in Figure 2d and Figure S1, indicating their dynamic stability. On the other hand, three thermodynamically stable B-site-ordered compounds in the $Fm\overline{3}m$ symmetry ($Ca_6NPSb_2$, $Ca_6NPBi_2$ and $Sr_6NPBi_2$) display imaginary modes (with frequencies close to -1.5 THz at the Γ and X points) in the phonon spectra (Figure S2), suggesting dynamic instability. For ideal cubic perovskites $ABX_3$ and double perovskites $A_2BB'X_6$, their distorted variants are common and can be more stable than the cubic prototype.[60-62] However, since studying crystal structural distortion for each compound with phonon instability is time-consuming, we first study the electronic properties of 21 thermodynamically stable compounds in $P4/mmm$ and $Fm\overline{3}m$ symmetries. If a compound with phonon instability is a potential candidate for photovoltaic applications on the basis of electronic properties, the structural distortion will be further studied.

### 3.2. Electronic Properties of Quaternary Antiperovskites with Thermodynamic Stability

We calculated the band structure of an experimentally available antiperovskite $Mg_3NSb$ using the HSE with 25% non-local Fock exchange and including the SOC effect. As shown in Figure S3, the calculated band gap (1.23 eV) of $Mg_3NSb$ agrees well with the experimental value (1.30 eV).[52] Therefore, we employed this method for the calculation of electronic properties of quaternary antiperovskites. As depicted in Figure 3a and Figure S4, the HSE+SOC calculated band structures of Mg-based A-site-ordered quaternary antiperovskites differ greatly from those of Ca- and Sr-based ones. Taking $X_6N_2SbBi$ (X=Mg, Ca, Sr) as examples, the $Mg_6N_2SbBi$ exhibits an indirect band gap with valence band maximum (VBM) at the Γ point and conduction band minimum (CBM) at the M point. In contrast, the VBM and the CBM of $Ca_6N_2SbBi$ and $Sr_6N_2SbBi$ are both located at the Γ point. Such a difference between the Mg and Ca/Sr compounds has also been found in antiperovskites ($Mg_3NA$ and $X'_3NA$ (X'=Ca, Sr, Ba; A=P, As, Sb, Bi)) and has been explained by the different hybridizations (the p-p hybridization in Mg-based compounds vs. the p-d hybridization in Ca/Sr/Ba-based compounds).[33] We note that $Mg_6N_2SbBi$ shows orbital and band valley degeneracy for the conduction band, denoting potential thermoelectric applications (more details about the Mg-based quaternary antiperovskites are given in the Supporting Information (Figure S5)).

Figure 3b shows the band gap variation of $X_6B_2AA'$ (X=Mg, Ca, Sr) as the AA' anionic combination changes. The band gaps vary in a wide range from 0.66 eV to 2.25 eV, suggesting possible diverse optoelectronic applications. One can see a general trend that the band gaps of $Mg_6N_2AA'$, $Ca_6N_2AA'$ and $Sr_6N_2AA'$ decrease as the total ionic radii of the AA' anionic combinations increase (r(PAs) < r(PSb) < r(AsSb) < r(PBi) < r(AsBi) < r(SbBi)). In addition, the band gaps decrease as the X-site element changes from Mg, to Ca and to Sr. Besides 18 A-site-ordered quaternary antiperovskites, the band structures of 3 B-site-ordered compounds ($Ca_6NPSb_2$, $Ca_6NPBi_2$ and $Sr_6NPBi_2$) are shown in Figure S6, which displays a similar chemical trend for the band gap, i.e., the band gap largely decreases from $Ca_6NPSb_2$ (Eg=1.14 eV) to $Ca_6NPBi_2$ (Eg=0.60 eV) and it also decreases as the X-site element varies from Ca to Sr ($Ca_6NPBi_2$ to $Sr_6NPBi_2$). These results show great band gap tunability of antiperovskites as a result of the compositional flexibility.

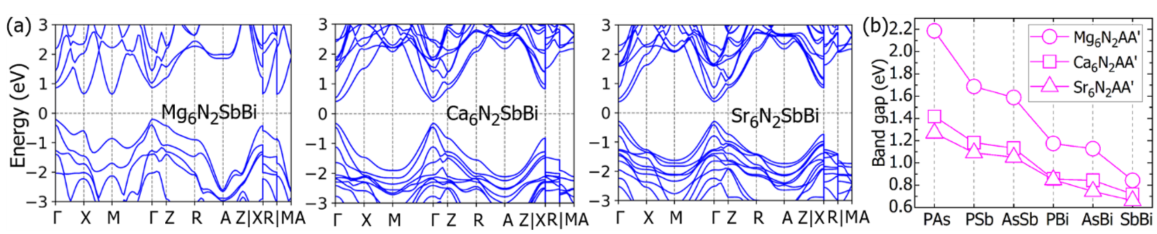


Figure 3. (a) Band structures of $X_6N_2SbBi$ (X=Mg, Ca, Sr) calculated at the HSE+SOC level. (b) Band gaps of $X_6N_2AA'$ (X=Mg, Ca, Sr; AA'= PAs, PSb, AsSb, PBi, AsBi, SbBi) quaternary antiperovskites calculated at the HSE+SOC level.

3.3. Identification of Ground-state Structures with Structural Distortion for Potential Quaternary Antiperovskites as Photovoltaic Absorbers

Among the 21 compounds with thermodynamic stability, 6 A-site-ordered double perovskites ($Ca_6N_2PAs$, $Ca_6N_2PSb$, $Ca_6N_2AsSb$, $Sr_6N_2PAs$, $Sr_6N_2PSb$ and $Sr_6N_2AsSb$) and 1 B-site-ordered compound ($Ca_6NPSb_2$) have suitable direct band gaps (within the range of 1.0-1.8 eV) and good band dispersion around band edges (as shown in Figure S4 and S6), indicating possible high carrier mobilities and potential as good photovoltaic absorber materials. The band gaps calculated by HSE are based on the crystal structures optimized by PBE calculations, which could lead to small underestimations of band gaps compared to those based on HSE-relaxed structures. We assumed either tetragonal or cubic structures for these compounds (see Section 3.1), but some of them are dynamically unstable as indicated by the presence of imaginary phonon modes (Figure S1 and Figure S2) despite being thermodynamically stable. Among the above 7 compounds, only the distortion-free $Ca_6N_2AsSb$ (SG *P*4*/mmm*) shows dynamic stability. For the other 6 compounds, we searched for their ground-state perovskite structures with structural distortions by using the group-theoretical method since it successfully revealed the relationships between the distorted variants and the cubic perovskite (double perovskite) prototypes.[61, 63]

After taking all possible distortions (mainly the tilting of the corner-linked octahedral units, viz., in-plane and out-of-phase rotation) into account, the ground-state perovskite structures with dynamic phonon stability for the 6 compounds ($Ca_6N_2PAs$, $Ca_6N_2PSb$, $Sr_6N_2PAs$, $Sr_6N_2PSb$, $Sr_6N_2AsSb$ and $Ca_6NPSb_2$) were successfully identified. $Sr_6N_2PAs$ is taken as an example to show the identification of the ground-state structure of A-site-ordered compounds. There are 11 distorted variants for $Sr_6N_2PAs$ in the *P*4*/mmm* symmetry and the ground-state structure has the $Pmc2_1$ symmetry as shown in Table 1. (Note that the *Pm* symmetry in Table 1 is only slightly distorted from the $Pmc2_1$ symmetry,[64] resulting in a very small energy difference between the two symmetries). For $Ca_6N_2PAs$, $Ca_6N_2PSb$, $Sr_6N_2PSb$ and $Sr_6N_2AsSb$, their ground-state structures have the same $Pmc2_1$ symmetry as $Sr_6N_2PAs$ does; they all have dynamic phonon stability as depicted in Figure S7-8. A similar method is applied to B-site-ordered compound $Ca_6NPSb_2$ as well (see Table S2), its ground-state structure is in the $P2_1/c$ symmetry. We note that although $Ca_6NPSb_2$ in the *C*2*/c* symmetry is only slightly less stable by 0.62

meV/atom than that in the $P2_1/c$ symmetry, the former shows imaginary modes in the phonon spectrum (Figure S9b) and, therefore, is not considered further. The crystal structures of 7 promising quaternary antiperovskites are summarized in Table S3. Additionally, the $E_{hull}$ of the distorted compounds becomes more negative (see Table S3), revealing their thermodynamical stability. It is worthwhile to note that the octahedral distortion reduces $E_{hull}$ by 50 meV/atom for $Sr_6N_2PAs$, suggesting that some of the compounds considered as thermodynamically unstable ($E_{hull}$ > 25 eV/atom) in Figure 2 (based on undistorted structures) could be stable after introducing octahedral distortion.

Table 1. All possible structures of $Sr_6N_2PAs$ derived from the prototype (*P*4*/mmm* phase) with applying distortion models (in Glazer notation)[60] to the [$Sr_6N$] octahedra.

| Space group | Tilt pattern | $\Delta E$ (meV/atom)$^\dagger$ |
|---|---|---|
| $P4/mmm$ (No. 123) | $a^0a^0a^0$ | 0.000 |
| $P4/mbm$ (No. 127) | $a^0a^0c^+$ | -29.752 |
| $P4/nbm$ (No. 125) | $a^0a^0c^-$ | -27.191 |
| $Cmmm$ (No. 65) | $a^-b^0c^0$ | -27.366 |
| $Pmma$ (No. 51) | $a^-a^-c^0$ | -32.105 |
| $P2/m$ (No. 10) | $a^-b^-c^0$ | -32.105 |
| $C2/m$ (No. 12) | $a^-b^0c^-$ | -32.558 |
| $Amm2$ (No. 38) | $a^-b^0c^+$ | -37.877 |
| $Pmc2_1$ (No. 26) | $a^-a^-c^+$ | -49.600 |
| $P2/c$ (No. 13) | $a^-a^-c^-$ | -31.394 |
| $Pm$ (No. 6) | $a^-b^-c^+$ | -49.598 |
| $P\bar{1}$ (No. 2) | $a^-b^-c^-$ | -32.556 |

$^\dagger$ The $\Delta E$ is given by taking $Sr_6N_2PAs$ (SG *P*4*/mmm*) as reference.

### 3.4. Quaternary Antiperovskites as Potential High-Performance Lead-Free Photovoltaic Absorbers

Seven quaternary antiperovskites ($Ca_6N_2AsSb$ (SG *P*4*/mmm*), $Ca_6N_2PAs$ (SG $Pmc2_1$), $Ca_6N_2PSb$ (SG $Pmc2_1$), $Sr_6N_2PAs$ (SG $Pmc2_1$), $Sr_6N_2PSb$ (SG $Pmc2_1$), $Sr_6N_2AsSb$ (SG $Pmc2_1$) and $Ca_6NPSb_2$ (SG $P2_1/c$)) were selected as potential solar absorbers based on their stability and electronic structures. Besides these, the following criteria are employed to further select the promising photovoltaic absorber materials: (i) carrier effective masses ($m_h^*$ and $m_e^*$) smaller than the rest mass of an electron ($m_0$) (beneficial for ambipolar carriers transport and efficient carrier extraction), (ii) fast exciton dissociation, enabled by low exciton binding energy ($E_b$ < 100 meV), (iii) high optical absorption and dipole-allowed optical transitions in the visible light range. These criteria lead to the selection of 5 compounds (4 A-site-ordered compounds $Ca_6N_2AsSb$ (SG *P4/mmm*), $Ca_6N_2PSb$ (SG *Pmc*2$_1$), $Sr_6N_2AsSb$ (SG *Pmc*2$_1$), $Sr_6N_2PSb$ (SG *Pmc*2$_1$), and 1 B-site-ordered compound $Ca_6NPSb_2$ (SG *P*2$_1$/*c*)) as promising compounds with anticipated high-performance photovoltaic properties, as depicted in Figure 4a with detailed data summarized in Table S3. Band structures of these candidates are shown in Figure 5a-b and Figure S10. It is worthwhile to note that $m_h^*$ is much smaller than $m_e^*$ for $Ca_6N_2AsSb$, $Ca_6N_2PSb$ and $Ca_6NPSb_2$, which is rare for a semiconductor since the hole mobility is low in most conventional semiconductors.[65-67] Such a small $m_h^*$ may be induced by strong cation-anion and anion-anion interactions at the VBM while there are only cation-anion interactions at the CBM. For these 5 optimal quaternary antiperovskites, the optical absorption spectrum and the spectroscopic limited maximum efficiency (SLME) as a function of thickness of the absorber layer are further studied.

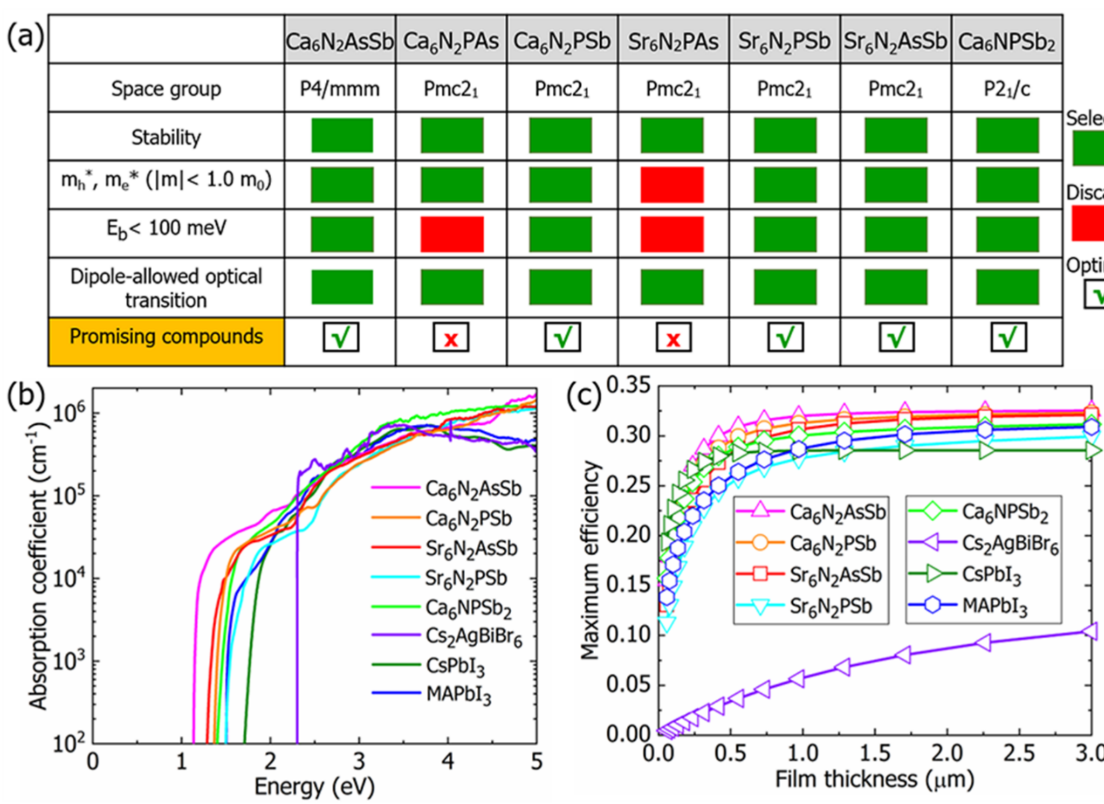

Figure 4. (a) Materials screening process on the basis of the properties relevant to photovoltaic performance, i.e., stability (thermodynamic and dynamic stability), carrier effective masses ($m_h^*$ and $m_e^*$), exciton binding energy ($E_b$) and dipole-allowed optical transitions. The green rectangles denote the materials passing the screening (Selected) and the red ones indicate not passing (Discarded). The optimal lead-free quaternary antiperovskites satisfying all the criteria are marked with green ticks. Meanwhile those with red cross are abandoned. (b) Calculated absorption spectra and (c) spectroscopic limited maximum efficiency of 5 optimal quaternary antiperovskites and three representative halide perovskites.

The suitable direct band gaps and dipole-allowed optical transitions lead to strong optical absorptions in the visible light range (1.65 eV to 3.10 eV) in the 5 promising quaternary antiperovskite compounds ($Ca_6N_2AsSb$, $Ca_6N_2PSb$, $Sr_6N_2AsSb$, $Sr_6N_2PSb$, and $Ca_6NPSb_2$), as shown in Figure 4b. The visible light absorption of these 5 compounds is much stronger than that of the halide double perovskite $Cs_2AgBiBr_6$ and is comparable to or even slightly higher than those in widely studied $CsPbI_3$ and $MAPbI_3$. Figure 4c shows the SLME of the 5 promising compounds and three halide perovskites as functions of the film thickness. The calculated maximum efficiency of a $Cs_2AgBiBr_6$ based solar cell with a 3 μm-thick film is 10.42%, which is in accordance with the previously calculated efficiency 10.5%.[68] Such a relatively low efficiency is partially attributed to the large indirect band gap of $Cs_2AgBiBr_6$.[25] In contrast to $Cs_2AgBiBr_6$, the 7 compounds shown in Figure 4c exhibit high conversion efficiencies. Remarkably, the SLME of $Ca_6N_2AsSb$, $Ca_6N_2PSb$, $Sr_6N_2AsSb$, $Sr_6N_2PSb$ and $Ca_6NPSb_2$ can reach predicted values as high as 32.53%, 32.32%, 32.12%, 29.94% and 31.17%, respectively, which are comparable to or even higher than those of $MAPbI_3$ (30.90%) and $CsPbI_3$ (28.55%). Strikingly, a high conversion efficiency of 25% can be achieved in very thin absorber layers with 0.3 μm thickness for quaternary antiperovskites $Ca_6N_2AsSb$, $Ca_6N_2PSb$, $Sr_6N_2AsSb$ and $Ca_6NPSb_2$, as shown in Figure 4c.

In halide double perovskites $Cs_2AgBiBr_6$ and $Cs_2AgInCl_6$, the A-site cation (Cs) plays little role in carrier transport, and there is nearly no overlap between the Ag and Bi (In) states at the VB and CB edges (Figure 5c-d), leading to the 0D character of electronic transport in $Cs_2AgBiBr_6$ and $Cs_2AgInCl_6$ although they both have 3D structural dimensionality at the sub-nanometer scale.[69] In contrast, all constituents contribute to the electronic states near the VBM and the cation states dominated the CBM in pnictogen-based quaternary antiperovskite compounds $Ca_6N_2AsSb$ (SG *P*4/*mmm*) and $Ca_6NPSb_2$ (SG *P*2$_1$/*c*) which are shown as examples (Figure 5a-b). Therefore, the electronic states near band edges in these quaternary antiperovskites are strongly hybridized in all three dimensions, resulting in efficient carrier transport in their 3D structures despite alternating cuboctahedra ([$Ca_{12}$A]/[$Ca_{12}$A']) or octahedra ([$Ca_6$B]/[$Ca_6$B']). Furthermore, as shown in Figure S11, mixing of cation p/d states with anion p states results in the filled antibonding and empty antibonding states at the upper valence band and lower conduction band for both $Ca_6N_2AsSb$ and $Ca_6NPSb_2$. Such a strong antibonding coupling could lead to highly dispersive band edges.

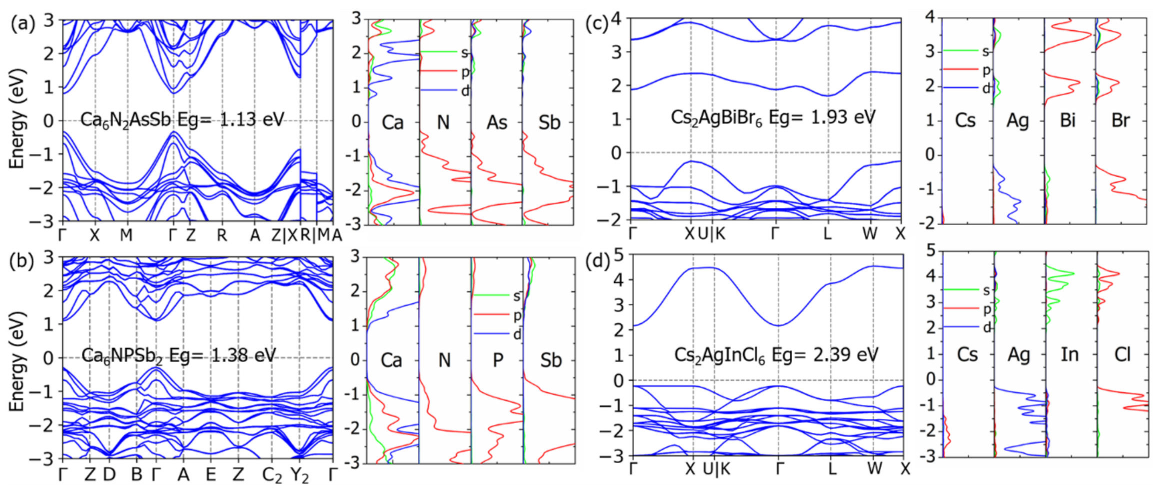


Figure 5. Band structures and density of states of (a) $Ca_6N_2AsSb$ (SG *P*4/*mmm*), (b) $Ca_6NPSb_2$ (SG *P*2$_1$/*c*), (c) $Cs_2AgBiBr_6$ and (d) $Cs_2AgInCl_6$.

### 3.5. Dielectric Properties

The calculation of the SLME above does not consider the effect of defects which can cause nonradiative carrier recombination and reduce the conversion efficiency of a solar cell. A detailed study of defect properties is beyond the scope of this work. However, previous works suggest that the strong dielectric screening contributes to the long carrier lifetime and diffusion length in $MAPbI_3$ based solar cells since dielectric screening reduces carrier scattering and trapping by charged defects and impurities.[70-71] Table 2 shows the large calculated static dielectric constants of the 5 promising quaternary antiperovskites, which are larger than those of halide perovskites and halide double perovskites, e.g., $CsPbI_3$, $Cs_2AgBiBr_6$ and $Cs_2AgInCl_6$. These results indicate possible efficient carrier transport in quaternary antiperovskites due to the strong screening of charged defects and impurities.

Table 2. Calculated static dielectric constants $\varepsilon_{st}$ (containing the ionic ($\varepsilon_{ion}$) and electronic ($\varepsilon_{\infty}$) contributions) of $Ca_6N_2AsSb$, $Ca_6N_2PSb$, $Sr_6N_2PSb$, $Sr_6N_2AsSb$, $Ca_6NPSb_2$, $Cs_2AgBiBr_6$, $Cs_2AgInCl_6$ and $CsPbI_3$. These are traces of the dielectric tensors.

| Compound | Space group | $\varepsilon_{ion}$ | $\varepsilon_{\infty}$ | $\varepsilon_{st}$ |
|---|---|---|---|---|
| $Ca_6N_2AsSb$ | $P4/mmm$ | 25.72 | 12.07 | 37.79 |
| $Ca_6N_2PSb$ | $Pmc2_1$ | 26.80 | 10.06 | 36.86 |
| $Sr_6N_2PSb$ | $Pmc2_1$ | 20.71 | 8.80 | 29.51 |
| $Sr_6N_2AsSb$ | $Pmc2_1$ | 24.61 | 10.12 | 34.73 |
| $Ca_6NPSb_2$ | $P2_1/c$ | 17.42 | 10.16 | 27.58 |
| $Cs_2AgBiBr_6$ | $Fm\bar{3}m$ | 11.48 | 4.86 | 16.34 |
| $Cs_2AgInCl_6$ | $Fm\bar{3}m$ | 7.51 | 3.74 | 11.25 |
| $CsPbI_3$ | $Pm\bar{3}m$ | 16.57 | 4.85 | 21.42 |

We further investigated the origin of the strong dielectric screening in quaternary antiperovskites. As tabulated in Table 2 and Table S4, the large static dielectric constants of the quaternary antiperovskites are dominated by the ionic contributions, and the Born charges of components in quaternary antiperovskites are enhanced compared to their nominal ionic charges (which are +2 for Ca, and -3 for pnictogen elements), which indicates strong lattice polarization. It is well known that the mixed ionic-covalent bonding character in many halides and oxides gives rise to large static dielectric constants and even ferroelectricity.[70, 72-74] Such bonding character is attributed to the special chemistry of $ns^2$ cations (e.g., $Pb^{2+}$, $Bi^{3+}$, $Tl^{+}$, $Sn^{2+}$, etc.), which are present in many excellent optoelectronic materials, such as $MAPbI_3$ and TlBr.[70, 75] Here, we use the electronic localization function (ELF) to characterize the level of electron localization and the bonding type.[76-77] In ELF plots, generally, cores, bonds, and lone pairs tend to be highlighted. As shown in Figure 6a-b, there are color variations between the Pb and I atoms, indicating electron local distributions; while no variational colors between the Cs and I denotes electron delocalized distributions. In one dimensional (1D) profile of ELF (Figure 6c), the ELF value for Cs-I bond has maxima near nuclei due to the strong localization of core and valence electrons, and is near zero in the non-nuclear region, which displays the character of a typical ionic bond.[76] On the other hand, the ELF value for the Pb-I bond in $CsPbI_3$ has a minimum well above zero near the non-nuclear region, indicating a mixed ionic-covalent character. For the quaternary antiperovskites $Ca_6N_2AsSb$ and $Ca_6NPSb_2$, as shown in Figure 6d-e and Figure 6g-h, there are variational colors between cation and anion and even anion and anion. Moreover, as depicted in Figure 6f and Figure 6i, ELF values of the minima near the non-nuclear region are above zero for both X-A/A' and X-B/B' bonds, in contrast to $CsPbI_3$, in which only the Pb-I (B-X) bond displays such a character. This ELF analysis in combination with the crossed band gap hybridization of the cation states (shown in Figure 5) demonstrates the mixed ionic-covalent bonding character for all cation-anion bonds in quaternary antiperovskites, which is consistent with the large lattice polarization and static dielectric constants shown in Table 2.

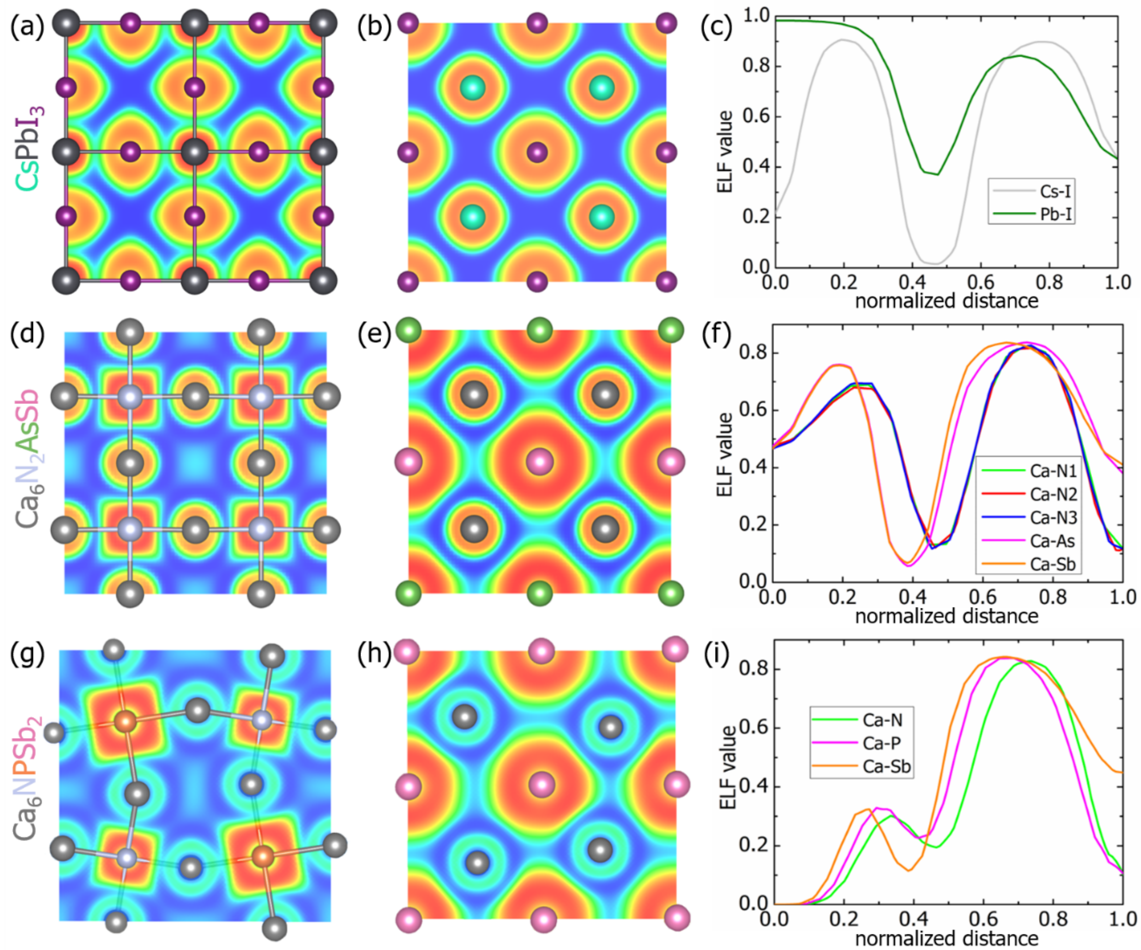


Figure 6. 2D Electron localization function (ELF) contours and 1D profile of ELF along the corresponding bonds of (a-c) $CsPbI_3$, (d-f) $Ca_6N_2AsSb$ and (g-i) $Ca_6NPSb_2$. Corresponding color code for constituents are shown on the left of Figure 6a, d and g.

### 3.6. Effect of Anion Disorder

Splitting A or B-site cation with isovalent elements has been used as a common method for designing perovskite compounds with ferroelectricity.[54, 78] An A-site-cation-ordered quadruple perovskite $AA'_3B_4O_{12}$ ($A=Pb^{2+}$; $A'=Hg^{2+}$; $B=Ti^{4+}$) and a B-site-cation-ordered $Bi^{3+}{}_2Fe^{3+}Al^{3+}O_6$ double perovskite have been synthesized.[79-80] Furthermore, a B-site-ordered double antiperovskite $Li_6O^{2-}S^{2-}I_2$ has also been successfully synthesized. These experimental results suggest that the ordering of two isovalent ions on either A or B site is possible. Nevertheless, we discuss anion disorder here since the impact of cation disorder on the band gap and a possible $V_{oc}$ deficit has been reported in some photovoltaic absorber materials, such as $Cu_2ZnSnS_4$ and $ZnSnN_2$.[81-83] We investigated the anion disorder effect on two promising candidates (A-site-ordered $Ca_6N_2AsSb$ (SG $P4/mmm$) and B-site-ordered $Ca_6NPSb_2$ (SG $P2_1/c$)) by the SQS method which represents maximal disorder.

For the A-site-ordered compound $Ca_6N_2AsSb$, the energy difference between the ordered and disordered supercells is close to zero, suggesting the possibility of forming solid solutions of $Ca_3NAs_xSb_{1-x}$. On the other hand, the B-site-ordered compound $Ca_6NPSb_2$ is 65 meV per mixed anion B-site lower in energy than the disordered one. Based on a simple regular solution model,[84] we estimated order/disorder transition temperatures of $Ca_6NPSb_2$ and $Cs_2AgBiBr_6$; they are 1093 K and 2372 K, respectively. The above simple estimation of the transition temperature of $Cs_2AgBiBr_6$ (2372 K) is reasonably close to the value (3000 K) determined by a Monte Carlo simulation.[85] Thus, whether a disorder can develop in $Ca_6NPSb_2$ depends on the growth temperature.

Next, we discuss the effect of disorder on electronic structure. We find that the disorder does not change the band gaps of $Ca_6N_2AsSb$ and $Ca_6NPSb_2$ significantly; the disorder-induced band gap increases are only 0.018 eV for the former and 0.087 eV for the latter. The effect of disorder on the effective masses is also moderate as shown in Table S5. Therefore, the anion disorder in $Ca_6N_2AsSb$ and $Ca_6NPSb_2$ is not expected to have a significant impact on optical and transport properties. The small effects of A- or B-site anion disorder on the electronic structures of quaternary antiperovskites can be understood by the significant contributions of both A and A' anions or both the B and B' anions to the orbital makeup of the valence band states, as shown in Figure 5. This is in contrast to the cases of $Cs_2AgBiBr_6$, $ZnSnN_2$, and $ZnSnP_2$,[83, 85-86] in which the cation disorder can affect electronic structure in a more profound way due to the dominant contribution of only one type of cation to the conduction or valence bands.

### 3.7. Comments on Materials Synthesis

It should be mentioned that our proposed compounds may not be solution processable as halide perovskites. The low-cost solution processing is a big advantage of halide perovskites, but it also naturally leads to hygroscopic materials that suffer from chemical instability.[5] Compared to lead halide perovskites, quaternary antiperovskites exhibit the characteristics of improved stability and no toxic elements. Meanwhile, we are aware of some previous works on synthesizing complex nitrides, which may give a clue on the synthesis of compounds predicted by us. For example, antiperovskite $Mg_3NSb$ thin films and ferroelectric nitride perovskite $LaWN_3$ thin films have been synthesized by sputter deposition; complex multinary nitrides $CaGaSiN_3$ and $CaAlSiN_3$: Eu have been synthesized by the ammonothermal method.[52, 55, 87-88]

## 4. CONCLUSIONS

New environmentally friendly pnictogen-based quaternary antiperovskites ($X_6B_2AA'$ and $X_6BB'A_2$) are designed for photovoltaic applications via ion type inversion in combination with the strategy of anion ordering. Through first-principles calculations, we systematically investigated their chemical and structural stabilities, electronic structure and photovoltaic related properties, and identified 5 stable quaternary antiperovskite compounds ($Ca_6N_2AsSb$, $Ca_6N_2PSb$, $Sr_6N_2AsSb$, $Sr_6N_2PSb$, and $Ca_6NPSb_2$) as promising photovoltaic absorber materials. These 5 compounds show predicted theoretical maximum solar cell efficiencies comparable to those of $MAPbI_3$ and $CsPbI_3$. The best-of-class compound $Ca_6NPSb_2$ exhibits a slightly higher predicted solar cell efficiency (31.17%) than that of $MAPbI_3$ (30.90%). Our work reveals the superior photovoltaic properties of pnictogen-based quaternary antiperovskites and opens a new avenue for designing lead-free and air-stable perovskite structure-based photovoltaic absorber materials.

## ASSOCIATED CONTENT

The Supporting Information is available free of charge on the XXX.

Energy above hull of $Ba_6BB'A_2$, phonon spectra of thermodynamically stable quaternary antiperovskites without and with octahedral distortions, band structures of $Mg_3NSb$ and quaternary antiperovskites with thermodynamic stability, schematic of band convergency of $Mg_6N_2AA'$, all possible structures of $Ca_6NPSb_2$ with distorted octahedra, explicit calculated data of all the candidates for materials screening, crystal orbital Hamilton population (COHP) analysis of $Ca_6N_2AsSb$ (SG $P4/mmm$) and $Ca_6NPSb_2$ (SG $P2_1/c$), calculated Born effective charge tensors, carrier effective masses of $Ca_6N_2AsSb$ and $Ca_6NPSb_2$ with anion disorder.

## AUTHOR INFORMATION

**Corresponding Authors**

Dan.Han@cup.uni-muenchen.de

gtang@uliege.be

**Conflict of Interest**

The authors declare no conflict of interest.

**Author Contributions**

The manuscript was written through contributions of all authors. All authors have given approval to the final version of the manuscript.

## ACKNOWLEDGMENTS

Dan Han, Hubert Ebert and Thomas Bein acknowledge financial support from Deutsche Forschungsgemeinschaft (DFG, German Research Foundation) under Germany's Excellence Strategy—EXC 2089/1—390776260. Dan Han thanks the support of Leibniz Supercomputing Centre of the Bavarian Academy of Sciences and Humanities. Thomas Bein thanks the support by the Solar Technologies go Hybrid (SolTech) funded by the Bavarian Ministry of Science and Art. Mao-Hua Du was supported by the U. S. Department of Energy, Office of Science, Basic Energy Sciences, Materials Sciences and Engineering Division. Shizhe Wang acknowledges the support by China Scholarship Council. Gang Tang acknowledges the support by the Consortium des Équipements de Calcul Intensif (CÉCI) that is funded by the Fonds de la Recherche Scientifique de Belgique (F.R.S.-FNRS) under Grant No. 2.5020.11 and by the Walloon Region. Dan Han thanks Prof. Shiyou Chen for helpful discussion.

## REFERENCES

1. Stranks, S. D.; Eperon, G. E.; Grancini, G.; Menelaou, C.; Alcocer, M. J. P.; Leijtens, T.; Herz, L. M.; Petrozza, A.; Snaith, H. J., Electron-Hole Diffusion Lengths Exceeding 1 Micrometer in an Organometal Trihalide Perovskite Absorber. *Science* **2013,** *342* (6156), 341-344.

2. Shi, D.; Adinolfi, V.; Comin, R.; Yuan, M.; Alarousu, E.; Buin, A.; Chen, Y.; Hoogland, S.; Rothenberger, A.; Katsiev, K.; Losovyj, Y.; Zhang, X.; Dowben, P. A.; Mohammed, O. F.; Sargent, E. H.; Bakr, O. M., Low Trap-State Density and Long Carrier Diffusion in Organolead Trihalide Perovskite Single Crystals. *Science* **2015,** *347* (6221), 519-522.

3. Jason J. Yoo, G. S., Matthew R. Chua, Tae Gwan Park, Yongli Lu, Fabian Rotermund,

Young-Ki Kim, Chan Su Moon, Nam Joong Jeon, Juan-Pablo Correa-Baena, Vladimir Bulović, Seong Sik Shin, Moungi G. Bawendi & Jangwon Seo, Efficient Perovskite Solar Cells via Improved Carrier Management. *Nature* **2021,** *590*, 587–593.

4. NREL Best Research-Cell Efficiencies. https://www.nrel.gov/pv/cell-efficiency.html (accessed Jan 04, 2021).

5. Ju, M.-G.; Chen, M.; Zhou, Y.; Dai, J.; Ma, L.; Padture, N. P.; Zeng, X. C., Toward Eco-Friendly and Stable Perovskite Materials for Photovoltaics. *Joule* **2018,** *2* (7), 1231-1241.

6. Fu, P.; Hu, S.; Tang, J.; Xiao, Z., Material Exploration via Designing Spatial Arrangement of Octahedral Units: A Case Study of Lead Halide Perovskites. *Front. Optoelectron.* **2021**, 1-8.

7. Awais, M.; Kirsch, R. L.; Yeddu, V.; Saidaminov, M. I., Tin Halide Perovskites Going Forward: Frost Diagrams Offer Hints. *ACS Mater. Lett.* **2021,** *3*, 299-307.

8. Jellicoe, T. C.; Richter, J. M.; Glass, H. F.; Tabachnyk, M.; Brady, R.; Dutton, S. n. E.; Rao, A.; Friend, R. H.; Credgington, D.; Greenham, N. C., Synthesis and Optical Properties of Lead-Free Cesium Tin Halide Perovskite Nanocrystals. *J. Am. Chem. Soc.* **2016,** *138* (9), 2941-2944.

9. Krishnamoorthy, T.; Ding, H.; Yan, C.; Leong, W. L.; Baikie, T.; Zhang, Z.; Sherburne, M.; Li, S.; Asta, M.; Mathews, N., Lead-Free Germanium Iodide Perovskite Materials for Photovoltaic Applications. *J. Mater. Chem. A* **2015,** *3* (47), 23829-23832.

10. Qiu, X.; Cao, B.; Yuan, S.; Chen, X.; Qiu, Z.; Jiang, Y.; Ye, Q.; Wang, H.; Zeng, H.; Liu, J., From Unstable $CsSnI_3$ to Air-Stable $Cs_2SnI_6$: A Lead-Free Perovskite Solar Cell Light Absorber with Bandgap of 1.48 eV and High Absorption Coefficient. *Sol. Energy Mater. Sol. Cells* **2017,** *159*, 227-234.

11. Ming, W.; Shi, H.; Du, M.-H., Large Dielectric Constant, High Acceptor Density, and Deep Electron Traps in Perovskite Solar Cell Material $CsGeI_3$. *J. Mater. Chem. A* **2016,** *4* (36), 13852-13858.

12. Filip, M. R.; Giustino, F., Computational Screening of Homovalent Lead Substitution in Organic–Inorganic Halide Perovskites. *J. Phys. Chem. C* **2016,** *120* (1), 166-173.

13. Körbel, S.; Marques, M. A.; Botti, S., Stability and Electronic Properties of New Inorganic Perovskites from High-Throughput Ab Initio Calculations. *J. Mater. Chem. C* **2016,** *4* (15), 3157-3167.

14. Volonakis, G.; Filip, M. R.; Haghighirad, A. A.; Sakai, N.; Wenger, B.; Snaith, H. J.; Giustino, F., Lead-Free Halide Double Perovskites via Heterovalent Substitution of Noble Metals. *J. Phys. Chem. Lett.* **2016,** *7* (7), 1254-1259.

15. Filip, M. R.; Hillman, S.; Haghighirad, A. A.; Snaith, H. J.; Giustino, F., Band Gaps of the Lead-Free Halide Double Perovskites $Cs_2BiAgCl_6$ and $Cs_2BiAgBr_6$ from Theory and Experiment. *J. Phys. Chem. Lett.* **2016,** *7* (13), 2579-2585.

16. Zhao, X. G.; Yang, J. H.; Fu, Y.; Yang, D.; Xu, Q.; Yu, L.; Wei, S. H.; Zhang, L., Design of Lead-Free Inorganic Halide Perovskites for Solar Cells via Cation-Transmutation. *J. Am. Chem. Soc.* **2017,** *139* (7), 2630-2638.

17. Zhao, X. G.; Yang, D.; Sun, Y.; Li, T.; Zhang, L.; Yu, L.; Zunger, A., Cu-In Halide Perovskite Solar Absorbers. *J. Am. Chem. Soc.* **2017,** *139* (19), 6718-6725.
18. Slavney, A. H.; Hu, T.; Lindenberg, A. M.; Karunadasa, H. I., A Bismuth-Halide Double Perovskite with Long Carrier Recombination Lifetime for Photovoltaic Applications. *J. Am. Chem. Soc.* **2016,** *138* (7), 2138-2141.
19. Greul, E.; Petrus, M. L.; Binek, A.; Docampo, P.; Bein, T., Highly Stable, Phase Pure $Cs_2AgBiBr_6$ Double Perovskite Thin Films for Optoelectronic Applications. *J. Mater. Chem. A* **2017,** *5* (37), 19972-19981.
20. McClure, E. T.; Ball, M. R.; Windl, W.; Woodward, P. M., $Cs_2AgBiX_6$ (X = Br, Cl): New Visible Light Absorbing, Lead-Free Halide Perovskite Semiconductors. *Chem. Mater.* **2016,** *28* (5), 1348-1354.
21. Bartel, C. J.; Clary, J. M.; Sutton, C.; Vigil-Fowler, D.; Goldsmith, B. R.; Holder, A. M.; Musgrave, C. B., Inorganic Halide Double Perovskites with Optoelectronic Properties Modulated by Sublattice Mixing. *J. Am. Chem. Soc.* **2020,** *142* (11), 5135-5145.
22. Zhang, T.; Cai, Z. H.; Chen, S., Chemical Trends in the Thermodynamic Stability and Bandgaps of 980 Halide Double Perovskites: A High-Throughput First-Principles Study. *ACS Appl. Mater. Interfaces* **2020,** *12* (18), 20680-20690.
23. Meng, W.; Wang, X.; Xiao, Z.; Wang, J.; Mitzi, D. B.; Yan, Y., Parity-Forbidden Transitions and Their Impact on the Optical Absorption Properties of Lead-Free Metal Halide Perovskites and Double Perovskites. *J. Phys. Chem. Lett.* **2017,** *8* (13), 2999-3007.
24. Xiao, Z.; Du, K.-Z.; Meng, W.; Wang, J.; Mitzi, D. B.; Yan, Y., Intrinsic Instability of $Cs_2In(I)M(III)X_6$ (M= Bi, Sb; X= Halogen) Double Perovskites: A Combined Density Functional Theory and Experimental Study. *J. Am. Chem. Soc.* **2017,** *139* (17), 6054-6057.
25. Savory C N, W. A., Scanlon D O, Can Pb-Free Halide Double Perovskites Support High-Effciency Solar Cells? *ACS Energy Lett.* **2016,** *1* (5), 949-955.
26. Du, K. z.; Meng, W.; Wang, X.; Yan, Y.; Mitzi, D. B., Bandgap Engineering of Lead - Free Double Perovskite $Cs_2AgBiBr_6$ through Trivalent Metal Alloying. *Angew. Chem. Int. Ed.* **2017,** *56* (28), 8158-8162.
27. Connor, B. A.; Leppert, L.; Smith, M. D.; Neaton, J. B.; Karunadasa, H. I., Layered Halide Double Perovskites: Dimensional Reduction of $Cs_2AgBiBr_6$. *J. Am. Chem. Soc.* **2018,** *140* (15), 5235-5240.
28. Lamba, R. S.; Basera, P.; Bhattacharya, S.; Sapra, S., Band Gap Engineering in $Cs_2(Na_xAg_{1-x})BiCl_6$ Double Perovskite Nanocrystals. *J. Phys. Chem. Lett.* **2019,** *10* (17), 5173-5181.
29. Wang, B.; Li, N.; Yang, L.; Dall'Agnese, C.; Jena, A. K.; Sasaki, S.-i.; Miyasaka, T.; Tamiaki, H.; Wang, X.-F., Chlorophyll Derivative-Sensitized $TiO_2$ Electron Transport Layer for Record Efficiency of $Cs_2AgBiBr_6$ Double Perovskite Solar Cells. *J. Am. Chem. Soc.* **2021,** *143* (5), 2207-2211.
30. Gebhardt, J.; Rappe, A. M., Adding to the Perovskite Universe: Inverse-Hybrid Perovskites.

*ACS Energy Lett.* **2017,** *2* (12), 2681-2685.
31. Gebhardt, J.; Rappe, A. M., Design of Metal-Halide Inverse-Hybrid Perovskites. *J. Phys. Chem. C* **2018,** *122* (25), 13872-13883.
32. Wang, Y.; Zhang, H.; Zhu, J.; Lü, X.; Li, S.; Zou, R.; Zhao, Y., Antiperovskites with Exceptional Functionalities. *Adv. Mater.* **2020,** *32* (7), 1905007.
33. Mochizuki, Y.; Sung, H.-J.; Takahashi, A.; Kumagai, Y.; Oba, F., Theoretical Exploration of Mixed-Anion Antiperovskite Semiconductors $M_3XN$ (M= Mg, Ca, Sr, Ba; X= P, as, Sb, Bi). *Phys. Rev. Mater.* **2020,** *4* (4), 044601.
34. Dai, J.; Ju, M.-G.; Ma, L.; Zeng, X. C., Bi(Sb)$NCa_3$: Expansion of Perovskite Photovoltaics into All-Inorganic Anti-Perovskite Materials. *J. Phys. Chem. C* **2019,** *123* (11), 6363-6369.
35. Goh, W. F.; Pickett, W. E., Survey of the Class of Isovalent Antiperovskite Alkaline-Earth Pnictide Compounds. *Phys. Rev. B.* **2018,** *97* (3), 035202.
36. Beznosikov, B., Predicted Nitrides with an Antiperovskite Structure. *J. Struct. Chem.* **2003,** *44* (5), 885-888.
37. Sreedevi, P.; Vidya, R.; Ravindran, P., Earth-Abundant Nontoxic Direct Band Gap Semiconductors for Photovoltaic Applications by Ab-Initio Simulations. *Sol. Energy* **2019,** *190*, 350-360.
38. Wang, Z.; Xu, H.; Xuan, M.; Shao, G., From Anti-Perovskite to Double Anti-Perovskite: Tuning Lattice Chemistry to Achieve Super-Fast $Li^+$ Transport in Cubic Solid Lithium Halogen–Chalcogenides. *J. Mater. Chem. A* **2018,** *6* (1), 73-83.
39. Kresse, G.; Furthmuller, J., Efficient Iterative Schemes for Ab Initio Total-Energy Calculations Using a Plane-Wave Basis Set. *Phys. Rev. B.* **1996,** *54* (16), 11169-11186.
40. Perdew, J. P.; Burke, K.; Ernzerhof, M., Generalized Gradient Approximation Made Simple. *Phys. Rev. Lett.* **1996,** *77* (18), 3865.
41. Heyd, J.; Scuseria, G. E.; Ernzerhof, M., Hybrid Functionals Based on a Screened Coulomb Potential. *J. Chem. Phys.* **2003,** *118* (18), 8207-8215.
42. Xiao, Z.; Meng, W.; Wang, J.; Yan, Y., Thermodynamic Stability and Defect Chemistry of Bismuth-Based Lead-Free Double Perovskites. *ChemSusChem* **2016,** *9* (18), 2628-2633.
43. Han, D.; Ogura, M.; Held, A.; Ebert, H., Unique Behavior of Halide Double Perovskites with Mixed Halogens. *ACS Appl. Mater. Interfaces* **2020,** *12* (33), 37100-37107.
44. Wang, V.; Xu, N.; Liu, J.-C.; Tang, G.; Geng, W.-T., Vaspkit: A User-Friendly Interface Facilitating High-Throughput Computing and Analysis Using Vasp Code. *Comput. Phys. Commun.* **2021**, 108033.
45. Jain, A.; Shyue Ping, O.; Hautier, G.; Chen, W.; Richards, W. D.; Dacek, S.; Cholia, S.; Gunter, D.; Skinner, D.; Ceder, G.; Persson, K. A., Commentary: The Materials Project: A Materials Genome Approach to Accelerating Materials Innovation. *APL Mater.* **2013,** *1* (1), 011002.
46. Togo, A.; Tanaka, I., First Principles Phonon Calculations in Materials Science. *Scripta Mater.* **2015,** *108*, 1-5.

47. Alexandr Fonari, C. S. *Effective Mass Calculator*, V1; GitHub repository: https://github.com/afonari/emc, 2012.
48. Jong, U.-G.; Yu, C.-J.; Ri, J.-S.; Kim, N.-H.; Ri, G.-C., Influence of Halide Composition on the Structural, Electronic, and Optical Properties of Mixed $CH_3NH_3Pb(I_{1-x}Br_x)_3$ Perovskites Calculated Using the Virtual Crystal Approximation Method. *Phys. Rev. B.* **2016,** *94* (12), 125139.
49. Yu, L.; Zunger, A., Identification of Potential Photovoltaic Absorbers Based on First-Principles Spectroscopic Screening of Materials. *Phys. Rev. Lett.* **2012,** *108* (6), 068701.
50. Logan, W.; Michael, W. *SL3ME*, V1; GitHub repository: https://github.com/ldwillia/SL3ME, 2018.
51. Zunger, A.; Wei, S.; Ferreira, L. G.; Bernard, J. E., Special Quasirandom Structures. *Phys. Rev. Lett.* **1990,** *65* (3), 353-356.
52. Heinselman, K. N.; Lany, S.; Perkins, J. D.; Talley, K. R.; Zakutayev, A., Thin Film Synthesis of Semiconductors in the Mg–Sb–N Materials System. *Chem. Mater.* **2019,** *31* (21), 8717-8724.
53. King, G.; Woodward, P. M., Cation Ordering in Perovskites. *J. Mater. Chem.* **2010,** *20* (28), 5785-5796.
54. Gou, G.; Young, J.; Liu, X.; Rondinelli, J. M., Interplay of Cation Ordering and Ferroelectricity in Perovskite Tin Iodides: Designing a Polar Halide Perovskite for Photovoltaic Applications. *Inorg. Chem.* **2017,** *56* (1), 26-32.
55. Talley, K. R.; Perkins, C. L.; Diercks, D. R.; Brennecka, G. L.; Zakutayev, A. Synthesis of Ferroelectric $LaWN_3$-the First Nitride Perovskite. 2020, arXiv:2001.00633. arXiv.org. https://arxiv.org/abs/2001.00633 (accessed June 15, 2021).
56. Li, C.; Lu, X.; Ding, W.; Feng, L.; Gao, Y.; Guo, Z., Formability of $ABX_3$ (X= F, Cl, Br, I) Halide Perovskites. *Acta Crystallogr. Sect. B: Struct. Sci.* **2008,** *64* (6), 702-707.
57. Kumar, A.; Verma, A.; Bhardwaj, S., Prediction of Formability in Perovskite-Type Oxides. *Prediction of Formability in Perovskite-Type Oxides* **2008,** *1* (1), 11-19.
58. Lu, Z.; Liu, J.; Ciucci, F., Superionic Conduction in Low-Dimensional-Networked Anti-Perovskites. *Energy Stor. Mater.* **2020,** *28*, 146-152.
59. Dawson, J. A.; Attari, T. S.; Chen, H.; Emge, S. P.; Johnston, K. E.; Islam, M. S., Elucidating Lithium-Ion and Proton Dynamics in Anti-Perovskite Solid Electrolytes. *Energy Environ. Sci.* **2018,** *11* (10), 2993-3002.
60. Glazer, A., The Classification of Tilted Octahedra in Perovskites. *Acta Crystallogr., Sect. B: Struct. Crystallogr. Cryst. Chem.* **1972,** *28* (11), 3384-3392.
61. Howard, C. J.; Kennedy, B. J.; Woodward, P. M., Ordered Double Perovskites–a Group-Theoretical Analysis. *Acta Crystallogr. Sect. B: Struct. Sci.* **2003,** *59* (4), 463-471.
62. Flerov, I.; Gorev, M.; Aleksandrov, K.; Tressaud, A.; Grannec, J.; Couzi, M., Phase Transitions in Elpasolites (Ordered Perovskites). *Mater. Sci. Eng. R Rep.* **1998,** *24* (3), 81-151.
63. Howard, C. J.; Zhang, Z., Structure for Perovskites with Layered Ordering of a-Site Cations. *Acta Crystallogr. Sect. B: Struct. Sci.* **2004,** *60* (2), 249-251.

64. Stokes, H. T.; Hatch, D. M., Findsym: Program for Identifying the Space-Group Symmetry of a Crystal. *J. Appl. Crystallogr.* **2005,** *38* (1), 237-238.
65. Janotti, A.; Van de Walle, C. G., Fundamentals of Zinc Oxide as a Semiconductor. *Rep. Prog. Phys.* **2009,** *72* (12), 126501.
66. Nainani, A.; Bennett, B. R.; Brad Boos, J.; Ancona, M. G.; Saraswat, K. C., Enhancing Hole Mobility in III-V Semiconductors. *J. Appl. Phys.* **2012,** *111* (10), 103706.
67. Han, D.; Ebert, H., Identification of Potential Optoelectronic Applications for Metal Thiophosphates. *ACS Appl. Mater. Interfaces* **2021,** *13* (3), 3836-3844.
68. Palummo, M.; Berrios, E.; Varsano, D.; Giorgi, G., Optical Properties of Lead-Free Double Perovskites by Ab Initio Excited-State Methods. *ACS Energy Lett.* **2020,** *5* (2), 457-463.
69. Xiao, Z.; Meng, W.; Wang, J.; Mitzi, D. B.; Yan, Y., Searching for Promising New Perovskite-Based Photovoltaic Absorbers: The Importance of Electronic Dimensionality. *Mater. Horiz.* **2017,** *4* (2), 206-216.
70. Du, M. H., Efficient Carrier Transport in Halide Perovskites: Theoretical Perspectives. *J. Mater. Chem. A* **2014,** *2* (24), 9091-9098.
71. Juarez-Perez, E. J.; Sanchez, R. S.; Badia, L.; Garcia-Belmonte, G.; Kang, Y. S.; Mora-Sero, I.; Bisquert, J., Photoinduced Giant Dielectric Constant in Lead Halide Perovskite Solar Cells. *J. Phys. Chem. Lett.* **2014,** *5* (13), 2390-2394.
72. Han, D.; Shi, H.; Ming, W.; Zhou, C.; Ma, B.; Saparov, B.; Ma, Y.-Z.; Chen, S.; Du, M.-H., Unraveling Luminescence Mechanisms in Zero-Dimensional Halide Perovskites. *J. Mater. Chem. C* **2018,** *6*, 6398-6405.
73. Du, M.-H.; Singh, D. J., Enhanced Born Charges in III-VII, IV-$VII_2$, and V-$VII_3$ Compounds. *Phys. Rev. B.* **2010,** *82* (4), 045203.
74. Ghosez, P.; Michenaud, J.-P.; Gonze, X., Dynamical Atomic Charges: The Case of $ABO_3$ Compounds. *Phys. Rev. B.* **1998,** *58* (10), 6224.
75. Du, M.-H.; Singh, D. J., Enhanced Born Charge and Proximity to Ferroelectricity in Thallium Halides. *Phys. Rev. B.* **2010,** *81* (14), 144114.
76. Becke, A. D.; Edgecombe, K. E., A Simple Measure of Electron Localization in Atomic and Molecular Systems. *J. Chem. Phys.* **1990,** *92* (9), 5397-5403.
77. Silvi, B.; Savin, A., Classification of Chemical Bonds Based on Topological Analysis of Electron Localization Functions. *Nature* **1994,** *371* (6499), 683-686.
78. Mulder, A. T.; Benedek, N. A.; Rondinelli, J. M.; Fennie, C. J., Turning $ABO_3$ Antiferroelectrics into Ferroelectrics: Design Rules for Practical Rotation‐Driven Ferroelectricity in Double Perovskites and $A_3B_2O_7$ Ruddlesden‐Popper Compounds. *Adv. Funct. Mater.* **2013,** *23* (38), 4810-4820.
79. Zhao, J.; Gao, J.; Li, W.; Qian, Y.; Shen, X.; Wang, X.; Shen, X.; Hu, Z.; Dong, C.; Huang, Q., A Combinatory Ferroelectric Compound Bridging Simple $ABO_3$ and a-Site-Ordered Quadruple Perovskite. *Nat. Commun.* **2021,** *12* (1), 1-9.

80. De, C.; Arévalo‐López, Á. M.; Orlandi, F.; Manuel, P.; Attfield, J. P.; Sundaresan, A., Isovalent Cation Ordering in the Polar Rhombohedral Perovskite $Bi_2FeAlO_6$. *Angew. Chem.* **2018,** *130* (49), 16331-16335.
81. Wallace, S. K.; Frost, J. M.; Walsh, A., Atomistic Insights into the Order–Disorder Transition in $Cu_2ZnSnS_4$ Solar Cells from Monte Carlo Simulations. *J. Mater. Chem. A* **2019,** *7* (1), 312-321.
82. Chen, S.; Walsh, A.; Yang, J.-H.; Gong, X. G.; Sun, L.; Yang, P.-X.; Chu, J.-H.; Wei, S.-H., Compositional Dependence of Structural and Electronic Properties of $Cu_2ZnSn(S,Se)_4$ Alloys for Thin Film Solar Cells. *Phys. Rev. B.* **2011,** *83* (12), 125201.
83. Veal, T. D.; Feldberg, N.; Quackenbush, N. F.; Linhart, W. M.; Scanlon, D. O.; Piper, L. F.; Durbin, S. M., Band Gap Dependence on Cation Disorder in $ZnSnN_2$ Solar Absorber. *Adv. Energy Mater.* **2015,** *5* (24), 1501462.
84. Wei, S.-H.; Ferreira, L.; Zunger, A., First-Principles Calculation of Temperature-Composition Phase Diagrams of Semiconductor Alloys. *Phys. Rev. B.* **1990,** *41* (12), 8240.
85. Yang, J.; Zhang, P.; Wei, S.-H., Band Structure Engineering of $Cs_2AgBiBr_6$ Perovskite through Order–Disordered Transition: A First-Principle Study. *J. Phys. Chem. Lett.* **2018,** *9* (1), 31-35.
86. Scanlon, D. O.; Walsh, A., Bandgap Engineering of $ZnSnP_2$ for High-Efficiency Solar Cells. *Appl. Phys. Lett.* **2012,** *100* (25), 251911.
87. Li, J.; Watanabe, T.; Wada, H.; Setoyama, T.; Yoshimura, M., Low-Temperature Crystallization of Eu-Doped Red-Emitting $CaAlSiN_3$ from Alloy-Derived Ammonometallates. *Chem. Mater.* **2007,** *19* (15), 3592-3594.
88. Häusler, J.; Neudert, L.; Mallmann, M.; Niklaus, R.; Kimmel, A. C. L.; Alt, N. S.; Schlücker, E.; Oeckler, O.; Schnick, W., Ammonothermal Synthesis of Novel Nitrides: Case Study on $CaGaSiN_3$. *Chem. Eur. J.* **2017,** *23* (11), 2583-2590.